

LETTER TO THE EDITOR

# Transient MeV radiation from a relativistic tidal disruption candidate

Gor Oganessian<sup>1,2\*</sup>, Elias Kammoun<sup>3\*\*</sup>, Annarita Ierardi<sup>1,2\*\*\*</sup>, Alessio Ludovico De Santis<sup>1,2</sup>, Biswajit Banerjee<sup>1,2</sup>, Emanuele Sobacchi<sup>1,2</sup>, Felix Aharonian<sup>4,5,6</sup>, Samanta Macera<sup>1,2</sup>, Pawan Tiwari<sup>1,2</sup>, Alessio Mei<sup>1,2</sup>, Shraddha Mohnani<sup>7</sup>, Stefano Ascenzi<sup>1,2</sup>, Samuele Ronchini<sup>8,9</sup>, and Marica Branchesi<sup>1,2</sup>

<sup>1</sup> Gran Sasso Science Institute, Viale F. Crispi 7, L'Aquila (AQ), I-67100, Italy

<sup>2</sup> INFN - Laboratori Nazionali del Gran Sasso, L'Aquila (AQ), I-67100, Italy

<sup>3</sup> Cahill Center for Astronomy & Astrophysics, California Institute of Technology, Pasadena, CA 91125, USA

<sup>4</sup> Dublin Institute for Advanced Studies, 31 Fitzwilliam Place, Dublin 2, Ireland

<sup>5</sup> Max-Planck-Institut für Kernphysik, Saupfercheckweg 1, 69117 Heidelberg, Germany

<sup>6</sup> Yerevan State University, 1 Alek Manukyan St, Yerevan 0025, Armenia

<sup>7</sup> Department of Astronomy, Astrophysics and Space Engineering Indian Institute of Technology Indore, Simrol, Khandwa Road, Indore 453552, Madhya Pradesh, India

<sup>8</sup> Department of Astronomy and Astrophysics, The Pennsylvania State University, 525 Davey Lab, University Park, PA 16802, USA

<sup>9</sup> Institute for Gravitation & the Cosmos, The Pennsylvania State University, University Park, PA 16802, USA

Received xxx; accepted xxx

## ABSTRACT

On July 2, 2025, the Gamma-ray Burst Monitor (GBM) onboard the *Fermi* Gamma-ray space telescope detected three short-duration MeV transients with overlapping sky locations. These events, named as GRB 250702D, B, and E (collectively referred to as DBE), triggered the detector with delays of approximately 1–2 hours between each burst. Follow-up observations of this unusually long MeV transient (lasting >3 hours) by the *Neil Gehrels Swift Observatory* and the *Nuclear Spectroscopic Telescope Array* over a period of ~10 days revealed a steep temporal decline in soft X-rays ( $\propto t^{-1.9 \pm 0.1}$ ). These characteristics are consistent with the scenario in which DBE arises from a relativistic jet launched after the tidal disruption of a star by a compact object. In the relativistic Tidal Disruption Event (TDE) scenario, DBE is the first one with detected MeV  $\gamma$ -ray emission. We show that the time-resolved MeV spectra during the outbursts are best described by a single power-law,  $dN_\gamma/dE \propto E^{-1.5}$ , extending from 10 keV to 40 MeV. The upper limits at higher energies (> 100 MeV) indicate that the spectrum breaks at 10 – 100 MeV. From standard MeV  $\gamma$ -ray transparency arguments, we derive a lower limit on the jet bulk Lorentz factor. These constraints place DBE in the same category as four previously reported relativistic TDEs in terms of outburst luminosity and energetics. We discuss the origin of the MeV emission in several scenarios, including synchrotron and inverse Compton cooling of electrons accelerated in the jet.

**Key words.** radiation mechanisms: non-thermal – acceleration of particles – gamma rays: general – black hole physics – relativistic processes

## 1. Introduction

The Gamma-ray Burst Monitor (GBM) onboard the *Fermi* Gamma-ray Space Telescope detected and localized five Gamma-Ray Bursts (GRBs<sup>1</sup>) on July 2, 2025. Three of these MeV transients, namely GRB 250702D, B, and E (hereafter DBE), have overlapping sky positions, likely originating from the same source (Neights et al. 2025). The detection of hard X-ray emission from DBE was also reported by Konus-WIND (Frederiks et al. 2025), Swift-BAT/GUANO (DeLaunay et al. 2025) and the Space-based multi-band astronomical Variable Objects Monitor (SVOM; Svom/Grm Team et al. 2025). Soft X-ray detections spatially coincident with DBE were reported by the Einstein Probe (EP 250702A; Cheng et al. 2025) and the

Monitor of All-sky X-ray Image (Kawakubo et al. 2025), in observations preceding the first *Fermi*/GBM trigger.

Follow-up observations of EP 250702A/DBE by the X-Ray Telescope (XRT) onboard the *Neil Gehrels Swift Observatory* (*Swift*, hereafter) revealed an associated fast-declining soft X-ray transient ( $\propto t^{-2}$ ; Kennea et al. 2025). Observations by the *Nuclear Spectroscopic Telescope Array* (*NuSTAR*) in hard X-rays (3 – 79 keV), performed ~ 1 day after the trigger of DBE, were consistent with the steep decline in soft X-rays (O'Connor et al. 2025). A similar rapid decline was observed in the near-infrared (NIR; Levan et al. 2025).

The duration of DBE in the MeV phase (> 3 hours) significantly exceeds the typical timescales of classical GRBs (0.1 – 100 s). Its X-ray counterpart also evolves faster than typical GRB afterglows, where the luminosity decreases as  $\propto t^{-1}$  before the jet break (Mészáros & Rees 1997). These two basic observables (i.e., the prolonged MeV  $\gamma$ -ray emission and the steep X-ray decline) make DBE a strong candidate for a relativistic Tidal Disruption Event (TDE; Levan et al. 2025). Typically, during the tidal disruption of a star by a massive com-

\* e-mail: gor.oganessian@gssi.it

\*\* e-mail: ekammoun@caltech.edu

\*\*\* e-mail: annarita.ierardi@gssi.it

<sup>1</sup> Not all short-lasting MeV transients named as GRBs upon their trigger originate from classical GRB progenitors, such as collapsars and compact binary neutron star mergers.

pact object, the emitted flux drops as a power law proportional to  $t^{-5/3}$  (Rees 1988). The presence of hours-long outbursts preceding the classical steep decline phase suggests the formation of a relativistic jet. To date, only four relativistic TDEs have been identified: Swift J164449.3+573451 (Burrows et al. 2011; Bloom et al. 2011; Levan et al. 2011), Swift J2058.4+0516 (Cenko et al. 2012; Pasham et al. 2015), Swift J1112.2-8238 (Brown et al. 2015), and AT2022cmc (Andreoni et al. 2022; Pasham et al. 2023). These events were detected up to hard X-rays ( $< 200$  keV), but not in MeV  $\gamma$ -rays.

In this Letter, we investigate the high-energy radiation associated with DBE, from soft X-rays to  $\gamma$ -rays. We analyze each DBE outburst using publicly available data from *Fermi*/GBM (8 keV – 40 MeV) and *Fermi*/Large Area Telescope (LAT,  $> 100$  MeV). We also analyze the soft and hard X-ray emission of DBE in the first 10 days, provided by publicly available *Swift*/XRT observations, and a dedicated *NuSTAR* Director Discretionary Time (DDT) observation obtained by our team. We then briefly discuss the properties of the emission region, where the non-thermal  $\gamma$ -ray photons are produced.

## 2. Temporal profile

We extract the background-subtracted MeV light curve over a 5.5-hour interval following the trigger of 250702D (see the upper panel of Fig. 1 and Appendix A.1). The first two events, 250702D and 250702B, have similar durations of  $\sim 100 - 150$  s and are separated by a quiescent period of  $\sim 45$  minutes. A third associated burst, 250702E, occurred  $\sim 3$  hours later and lasted  $\sim 600$  s. Large parts of the intermediate temporal windows between these three events were not accessible due to Earth’s occultation. A weak emission episode at  $t \sim t_0 + 6000$  s originates from GRB 250702C (Fermi GBM Team 2025), which is not related to DBE (Neights et al. 2025).

We performed a time-resolved spectral analysis of the soft X-ray emission observed by *Swift*/XRT (0.3 – 10 keV) and *NuSTAR* (Harrison et al. 2013) over the period from 0.5 to 10 days post-trigger of 250702D. The details of the spectral analysis are presented in Appendix B. The X-ray light curve shows a steep temporal decline, following  $t^{-1.9 \pm 0.1}$  (lower panel of Fig. 1).

## 3. $\gamma$ -ray spectra

We extract the *Fermi*/GBM spectra during the three emission episodes (D, B, and E) from the daily GBM data. The background spectra for the short episodes (D and B) are estimated using standard polynomial fits to time intervals before and after each burst. To evaluate the background during the long-duration episode E, we adopt the average orbital method. Details of GBM data extraction and analysis are provided in Appendix A.2.

We first model the spectra of episodes D, B, and E using a simple power-law (PL) model,  $dN/dE \propto E^{-\alpha}$  (Fig. 2). The best fit to the data in the energy range between 10 keV (40 keV for E) and 40 MeV provides  $\alpha = 1.5 \pm 0.1$  for D and B, and a slightly softer spectrum for E ( $\alpha = 1.64 \pm 0.04$ ).

We then test for the presence of a high-energy softening by fitting the spectra with a cutoff power-law (CPL) model. We find no significant improvement in the fit compared to the simple PL model. The cutoff energy is poorly constrained in all cases:  $E_{\text{cut}} > 4$  MeV for D,  $E_{\text{cut}} = 7_{-6}^{+13}$  MeV for B, and  $E_{\text{cut}} > 14$  MeV for E. We compare the best-fit CPL models with the  $3\sigma$  upper

<sup>2</sup>  $t_0$  is defined as the trigger time of 250702D, on 2025-07-02 13:09:02.03 (UT).

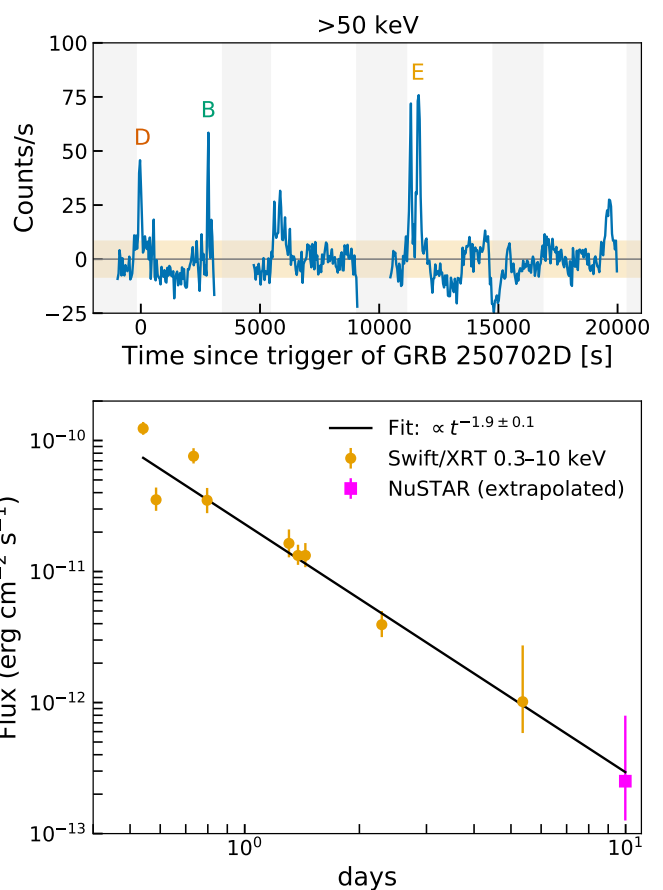


Fig. 1: Upper panel: Background-subtracted 5 s-binned light curve of the hard X-rays/MeV emission detected by *Fermi*/GBM (50 – 900 keV). Gray shaded regions indicate time bins during which the source was occulted by the Earth. The yellow shaded region marks  $1\sigma$  noise level in the light curve. Lower panel: Light curve of the soft X-ray counterpart obtained from time-resolved spectral analysis of *Swift*/XRT (0.3–10 keV, yellow circles). The flux at 0.3 – 10 keV at 10 days (pink square) was estimated by extrapolating the spectral model fitted to the *NuSTAR* data (fitted in the 3 – 30 keV range).

limits from *Fermi*/LAT at 0.1 – 1 GeV (see Appendix C). These upper limits suggest that the cutoff energy should be between the GBM and LAT energy bands, i.e.  $10 \text{ MeV} < E_{\text{cut}} < 100 \text{ MeV}$ .

The spectra of episodes D and B are consistent in normalization and spectral shape. Above 200 keV, the background is well characterized by the average orbital method. Thus, we extract the cumulative D and B spectrum. Fitting it with a PL model returns  $\alpha = 1.77_{-0.12}^{+0.17}$ , indicating a possible softening at high energies.

## 4. Discussion

The particularly long duration ( $> 3$  hours) and variable MeV radiation is followed by a steep temporal decline in X-rays. The spectra in the MeV  $\gamma$ -rays are markedly different from those of classical GRBs. We find  $\alpha \sim 1.5$  or softer in DBE, as opposed to  $\alpha \sim 1$  in GRBs (Band et al. 1993). Moreover, the DBE spectra extend beyond  $\sim 0.1 - 1$  MeV, which is typical for both short and long GRBs. Provided the particularly long MeV duration and their spectral shape, together with the steep X-ray decline (0.5 – 10 days), we disfavor the origin via classical channels of

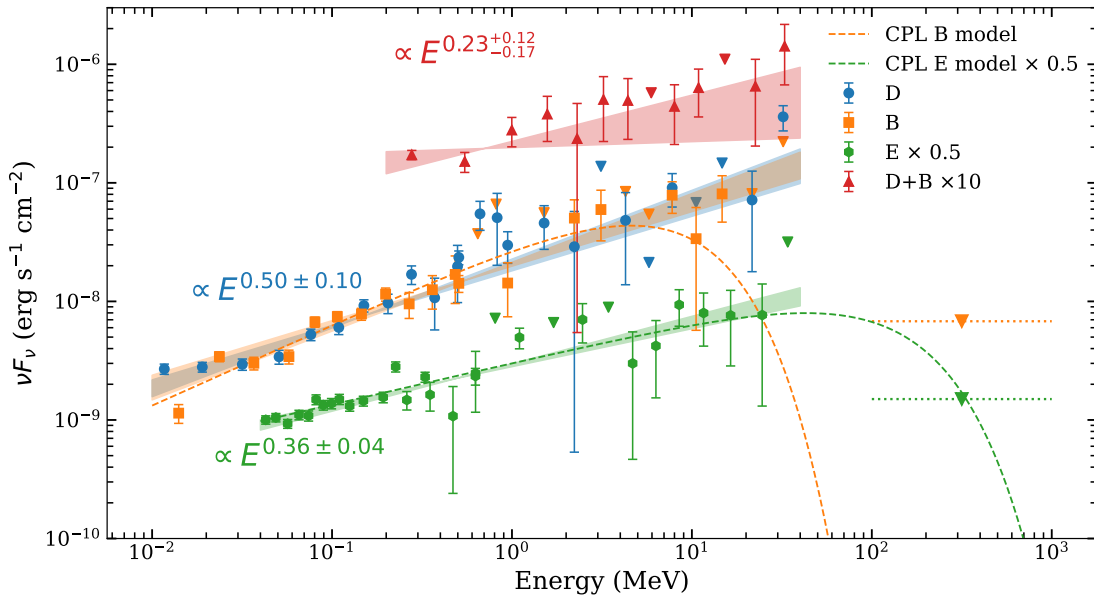


Fig. 2: Spectral energy distributions of events D, B, and E. The derived data points for the time-integrated spectra of D, B, and E, along with the best-fit power-law models (with  $1\sigma$  uncertainties) are shown using the blue, orange, and green symbols and shaded regions, respectively. The dashed orange and green lines represent average cutoff power-law models for the time-integrated spectra of events B and E. Upper limits between 100 MeV and 1 GeV ( $3\sigma$ ) are shown as inverted triangles. The combined D and B spectrum above 200 keV, along with its best-fit model ( $1\sigma$ ), is shown using red triangles and a red shaded region. The corresponding spectral slopes ( $2 - \alpha$ ) are also indicated.

formation of GRBs. Several arguments were put forward supporting the extragalactic origin of DBE (Levan et al. 2025), including its association with a candidate host galaxy of complex morphology. A transient relativistic jet formed as a consequence of the tidal disruption of a star by a compact object is a good candidate for long-duration MeV radiation. The previous four relativistic TDEs lack the emission in MeV  $\gamma$ -rays and were observed only up to hard X-rays ( $< 200$  keV). The absence of associated MeV radiation can be referred to the poor sensitivity of MeV instruments.

The individual outburst rise time and duration are linked to the density profile of the disrupted star and the mass of the compact object. It was previously argued that a variability time-scale of  $\sim 1000$  s implies that the disrupted star is most probably a white dwarf (Krolik & Piran 2011). The disruption of a white dwarf requires that the mass of the compact object is  $< 10^5 M_\odot$ . In the MeV  $\gamma$ -rays, DBE has even shorter observed variability of  $\sim 100 - 600$  s, which indicates that the compact object is an intermediate mass black hole (Levan et al. 2025).

#### 4.1. Constraints on the bulk Lorentz factor

We estimate a lower limit on the bulk Lorentz factor of the jet, assuming that the DBE emission is subject to the usual MeV compactness constraint<sup>3</sup>:

$$\Gamma > \left[ \frac{\eta(\beta)\sigma_T \left(\frac{\epsilon_{\max}}{2}\right)^{2\beta-1} (1+z)^{2\beta} d_L^2(z) F_0 (1-\beta)}{2\delta t_\nu m_e c^4 \left[1 - \left(\frac{\epsilon_0}{\epsilon_{\max}}\right)^{1-\beta}\right]} \right]^{\frac{1}{4+2\beta}}, \quad (1)$$

<sup>3</sup> Similar constraints were applied to classical GRBs in Ruderman (1975); Schmidt (1978); Lithwick & Sari (2001). See Ravasio et al. (2024) for more detailed derivations.

where  $\beta \sim 0.5$  is the spectral index ( $F_\nu \propto E^{-\beta}$ , where  $\beta = \alpha - 1$ ),  $\eta(\beta) = 7/6(2 + \beta)(1 + \beta)^{5/3}$  (Svensson 1987),  $\delta t_\nu \sim 100$  s is the observed variability time-scale,  $\epsilon_0 \sim 0.02$  and  $\epsilon_{\max} \sim 78$  are the minimum and maximum energies of the observed PL spectrum in units of the electron rest mass,  $F_0 \sim 3 \times 10^{-7}$  erg cm $^{-2}$  s $^{-1}$  is the flux integrated between  $\epsilon_0$  and  $\epsilon_{\max}$ , and  $z$  and  $d_L$  are the redshift and luminosity distance to the source, respectively.

In Fig. 3, we show the lower limit on the bulk Lorentz factor of the jet,  $\Gamma > 7d_{L,100\text{Mpc}}^{2/5}$ , as a function of the isotropic-equivalent outburst luminosity,  $L_{\text{iso}} \sim 4 \times 10^{47} d_{L,100\text{Mpc}}^2$  erg s $^{-1}$ , and source distance. We find that for  $\Gamma > 10$ , DBE is placed in the same category as the four previously reported jetted TDEs in terms of outburst luminosity.

The total fluence emitted during the three episodes across  $\epsilon_0 (\sim 0.02) - \epsilon_{\max} (\sim 78)$  is  $\sim 10^{-4}$  erg cm $^{-2}$ . Given the extension of the DBE spectra up to multi-MeV  $\gamma$ -rays ( $> 1$  MeV), the MeV emission provides a reasonable approximation of the total radiative energy budget. In Fig. D.1, we show  $\Gamma$  as a function of isotropic-equivalent energy. To match the energetics of the previously reported jetted TDEs, a value of  $\Gamma \sim 30$  is required. Combining our constraints on the luminosity of individual outbursts and the total energy budget, we conclude that  $10 < \Gamma < 30$  and  $100 \text{ Mpc} < d_L < 2 \text{ Gpc}$ , consistent with the redshift constraints from the host galaxy ( $z < 1$ ; Levan et al. 2025).<sup>4</sup>

The inferred photon index,  $\alpha \sim 1.5$ , can be produced by a cooled population of electrons with a distribution  $dN/d\gamma_e \propto \gamma_e^{-2}$ . We provide more details in Appendix D.

<sup>4</sup> In these estimates, we assume the jet is viewed on-axis. However, some TDE jets may be misaligned to account for late-time radio afterglow observations (Beniamini et al. 2023). If the DBE jet is misaligned, then the true Lorentz factor could be even larger.

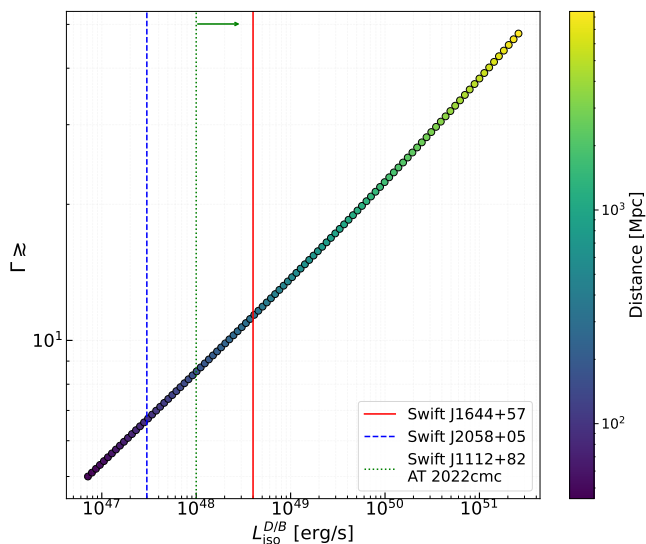


Fig. 3: Lower limit on the bulk Lorentz factor of the jet as a function of the isotropic-equivalent luminosity of the D and B emission episodes. The color bar indicates the corresponding luminosity distance to DBE. For comparison, we show the luminosity (brightest hard X-ray outbursts) measured for Swift J2058+05 (Cenko et al. 2012; Pasham et al. 2015), Swift J1112+82 (Brown et al. 2015), AT 2022cmc (Andreoni et al. 2022; Pasham et al. 2023), and Swift J1644+57 (Burrows et al. 2011) as dashed blue, dotted green, and solid red vertical lines.

## 5. Conclusions

We have presented a temporal and spectral analysis of GRB 250702D/B/E (DBE), three MeV transients with durations of 100 – 600 s, separated by  $\sim 1 - 3$  hours. The spatial coincidence of these events indicates a common origin, suggesting ultra-long central engine activity lasting more than 3 hours. Our findings can be summarized as follows:

- The prolonged MeV emission and the subsequent steep decline in the X-ray light curve in the first 10 days are different from classical GRBs, pointing instead to a TDE involving a relativistic jet.
- All three  $\gamma$ -ray episodes exhibit soft power-law spectra with indices  $\alpha$  ( $dN/dE \propto E^{-\alpha}$ ) ranging between 1.5 and 1.7 over the 10 keV – 40 MeV band, inconsistent with classical GRBs.
- The spectra of episodes D and B, separated by  $\sim 45$  minutes, are consistent in spectral shape and normalization.
- No significant high-energy cutoff is found within the 10 keV – 40 MeV range.
- The *Fermi*/LAT ( $E > 100$  MeV) upper limits during the B and E episodes suggest that the spectrum softens between 10 – 100 MeV. The combined D+B spectrum above 200 keV further supports the presence of a high-energy softening.
- The constraints on the bulk Lorentz factor place DBE in the same category as the four previously reported jetted TDEs in terms of outburst luminosity and energetics.

If DBE originated from a jetted TDE, it would represent the first such event with detected MeV emission. We have briefly discussed the origin of such emission, considering synchrotron and inverse Compton losses of non-thermal electrons accelerated in the relativistic jet (bulk Lorentz factor  $\Gamma \sim 10$ ).

*Acknowledgements.* We thank M.E. Rasio, P. Blasi, P. Jonker and A. Levan for the fruitful discussions. We thank Fiona Harrison, PI of *NuSTAR*, and the *NuSTAR* SOC team for scheduling the requested DDT observation. This research

has made use of data obtained through the High Energy Astrophysics Science Archive Research Center Online Service, provided by the NASA/Goddard Space Flight Center, and specifically, this work made use of public *Fermi*-GBM and *Fermi*-LAT data. This work made use of data supplied by the UK Swift Science Data Centre at the University of Leicester. This research is based on observations obtained with *NuSTAR*, a project led by the California Institute of Technology, managed by the Jet Propulsion Laboratory, and funded by the National Aeronautics and Space Administration. Data analysis was performed using the *NuSTAR* Data Analysis Software (NuSTARDAS), jointly developed by the ASI Science Data Center (SSDC, Italy) and the California Institute of Technology (USA).

## References

- Andreoni, I., Coughlin, M. W., Perley, D. A., et al. 2022, *Nature*, 612, 430
- Araud, K. A. 1996, in *Astronomical Society of the Pacific Conference Series*, Vol. 101, *Astronomical Data Analysis Software and Systems V*, ed. G. H. Jacoby & J. Barnes, 17
- Band, D., Matteson, J., Ford, L., et al. 1993, *ApJ*, 413, 281
- Beniamini, P., Piran, T., & Matsumoto, T. 2023, *MNRAS*, 524, 1386
- Biltzinger, B., Kunzweiler, F., Greiner, J., Toelge, K., & Burgess, J. Michael. 2020, *AA*, 640, A8
- Bloom, J. S., Giannios, D., Metzger, B. D., et al. 2011, *Science*, 333, 203
- Brown, G. C., Levan, A. J., Stanway, E. R., et al. 2015, *MNRAS*, 452, 4297
- Burrows, D. N., Kennea, J. A., Ghisellini, G., et al. 2011, *Nature*, 476, 421
- Cenko, S. B., Krimm, H. A., Horesh, A., et al. 2012, *ApJ*, 753, 77
- Cheng, H. Q., Zhao, G. Y., Zhou, C., et al. 2025, *GRB Coordinates Network*, 40906, 1
- De Santis, A. L. 2024, *Orbital Subtraction Tool - GBM*
- DeLaunay, J., Ronchini, S., Tohuvavohu, A., et al. 2025, *GRB Coordinates Network*, 40903, 1
- Fermi GBM Team. 2025, *GRB Coordinates Network*, 40885, 1
- Fitzpatrick, G., Connaughton, V., McBreen, S., & Tierney, D. 2011, *Uncovering low-level Fermi/GBM emission using orbital background subtraction*
- Frederiks, D., Lysenko, A., Ridnaia, A., et al. 2025, *GRB Coordinates Network*, 40914, 1
- Goldstein, A., Cleveland, W. H., & Kocevski, D. 2022, *Fermi GBM Data Tools: v1.1.1*
- Harrison, F. A., Craig, W. W., Christensen, F. E., et al. 2013, *ApJ*, 770, 103
- Kaastar, J. S. & Bleeker, J. A. M. 2016, *A&A*, 587, A151
- Kawakubo, Y., Serino, M., Negoro, H., et al. 2025, *GRB Coordinates Network*, 40910, 1
- Kennea, J. A., Siegel, M. H., Evans, P. A., et al. 2025, *GRB Coordinates Network*, 40919, 1
- Krolik, J. H. & Piran, T. 2011, *ApJ*, 743, 134
- Levan, A. J., Martín-Carrillo, A., Laskar, T., et al. 2025, *arXiv e-prints*, arXiv:2507.14286
- Levan, A. J., Tanvir, N. R., Cenko, S. B., et al. 2011, *Science*, 333, 199
- Lithwick, Y. & Sari, R. 2001, *ApJ*, 555, 540
- Meegan, C., Lichi, G., Bhat, P. N., et al. 2009, *ApJ*, 702, 791
- Mészáros, P. & Rees, M. J. 1997, *ApJ*, 476, 232
- Neights, E., Roberts, O. J., Burns, E., et al. 2025, *GRB Coordinates Network*, 40931, 1
- O'Connor, B., Pasham, D., Andreoni, I., & Hare, J. 2025, *GRB Coordinates Network*, 41014, 1
- Pasham, D. R., Cenko, S. B., Levan, A. J., et al. 2015, *ApJ*, 805, 68
- Pasham, D. R., Lucchini, M., Laskar, T., et al. 2023, *Nature Astronomy*, 7, 88
- Ravasio, M. E., Ghirlanda, G., & Ghisellini, G. 2024, *A&A*, 685, A166
- Rees, M. J. 1988, *Nature*, 333, 523
- Ruderman, M. 1975, in *Seventh Texas Symposium on Relativistic Astrophysics*, ed. P. G. Bergman, E. J. Fenyves, & L. Motz, Vol. 262, 164–180
- Schmidt, W. K. H. 1978, *Nature*, 271, 525
- Svensson, R. 1987, *MNRAS*, 227, 403
- Svom/Grm Team, Wang, C.-W., Zheng, S.-J., et al. 2025, *GRB Coordinates Network*, 40923, 1

## Appendix A: Fermi GBM data analysis

### Appendix A.1: Orbital background estimate

To accurately estimate the background for the three observed  $\gamma$ -ray transients, we employed a modified version of the OSV tool (De Santis 2024; Fitzpatrick et al. 2011). This method leverages the periodic orbital characteristics of the *Fermi* satellite. *Fermi* operates in 90-minute orbits and performs a rocking maneuver every two orbits to ensure full-sky coverage (Meegan et al. 2009). This pattern results in the satellite returning to the exact same celestial position every 15 orbits, and to the same position with identical pointing every 30 orbits. The OSV tool exploits this by estimating the background for long or faint MeV sources with the mean event rate observed by the Gamma-ray Burst Monitor (GBM) 15 or 30 orbits before and after the time of interest.

For the binned data, the background estimate  $R_{\text{bck}}(t_i, E_i)$  for an observed rate  $R(t_i, E_i)$  in a specific time and energy bin ‘i’ is given by:

$$R_{\text{bck}}(t_i, E_i) = \frac{R(t_i + 24 \text{ h}, E_i) + R(t_i - 24 \text{ h}, E_i)}{2}. \quad (\text{A.1})$$

This formula applies to the 15-orbit scenario. For the 30-orbit scenario, the time difference becomes larger. Furthermore, averaging over 14 and 16 orbits also provides a robust background estimate (Fitzpatrick et al. 2011). This is attributed to the near-identical detector position and pointing angles at these orbital intervals.

It is crucial to note that the effectiveness of the 15-orbit method for background estimation, particularly above 40 keV, is enhanced by the energy cutoff. Many potential point sources, which could introduce contamination, contribute predominantly below 100 keV (Biltzinger, B. et al. 2020). Consequently, for the majority of our energy bins, the position of the detectors is the dominant factor influencing the background, rather than subtle pointing variations.

Fig. A.1 illustrates the background estimates for the primary time intervals for detectors ‘nb’ and ‘b1’. A qualitative validation of the background estimation can be done by comparing the predicted and measured rates in regions immediately adjacent to the signal. A close match indicates a valid background estimate.

Analysis of the data reveals that the background estimated using the 30-orbit method generally aligns well with the measured rates. The sole exception is detector ‘nb’ during GRB B, where the 30-orbit estimate clearly overestimates the background. In this specific case, the 15-orbit estimate provides a much more accurate representation of the pre- and post-burst background.

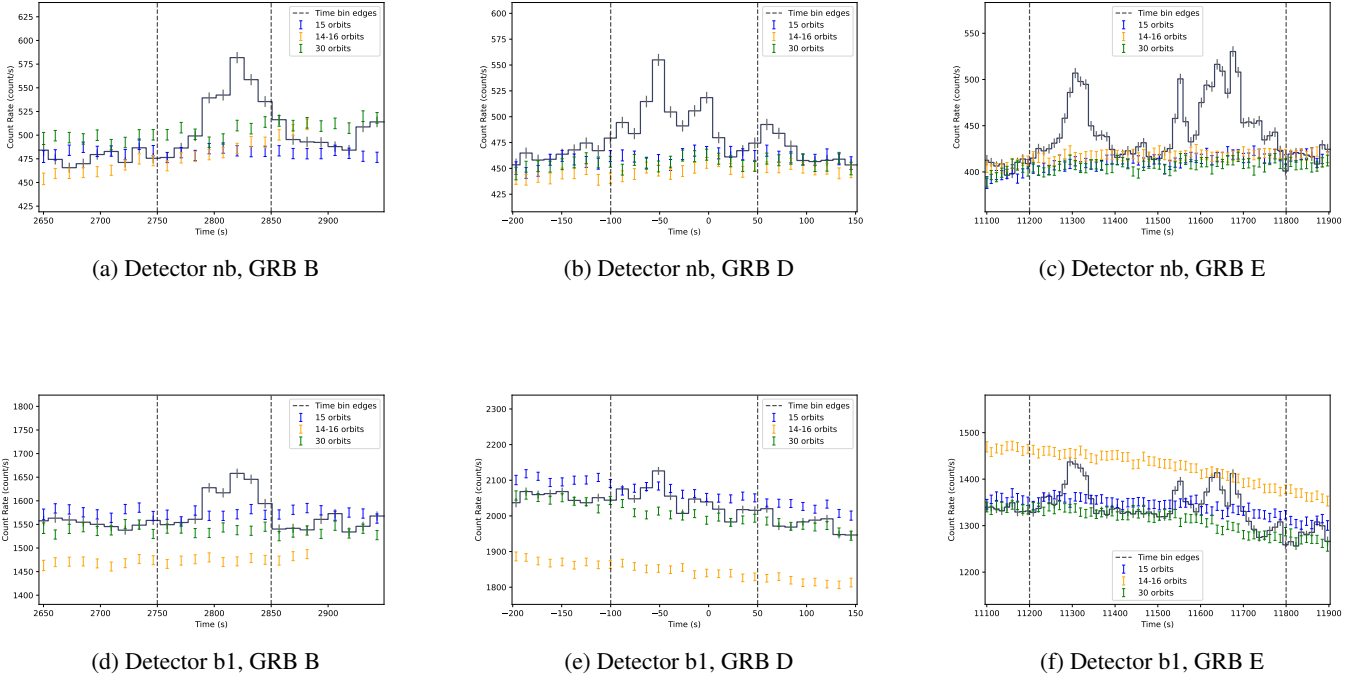


Fig. A.1: Light curves for two detectors (Detector nb: top row; Detector b1: bottom row) across three different events (Event 1: left column; Event 2: middle column; Event 3: right column). The estimated background is plotted using three different orbits. For the ‘nb’ data, the energy range is cut between 40 keV and 900 keV, while for ‘b1’ data, the cut is between 200 and 40000. Each panel shows the light curve integrated over energy for a specific detector and event combination.

### Appendix A.2: Spectral analysis

We first verified that during the temporal bins of the D, B, and E events, only one sodium iodide detector (nb) and one bismuth germanate detector (b1) satisfy the source-to-detector angle cuts. We downloaded the daily data for July 2, 2025, from the *Fermi*

GBM Daily Data online repository<sup>5</sup>. To analyze the time bins of interest, we generated response matrices using the GBM Response Generator<sup>6</sup>, based on the position provided by *Swift*/XRT. We identify the D, B, and E outburst times as  $-100$ – $50$  s,  $2750$ – $2850$  s, and  $11200$ – $11800$  s, respectively, since the trigger time of GRB 250702D (2 July 13:09:02.03 UT). We extracted the spectra from GBM daily data using the publicly available *Fermi* GBM Data Tools (Goldstein et al. 2022).

We tested two methods to estimate the background spectrum during the D, B, and E intervals (see below). The first method extrapolates a polynomial function fitted to pre- and post-burst intervals, allowing background estimation over the full *Fermi*/GBM energy range (10 keV – 40 MeV). The second method uses the average orbital background, which lacks coverage below 40 keV. The results of the spectral modeling are presented in Table A.1. We note that all spectral fits presented in this work are performed using XSPEC (Arnaud 1996), and assuming Cash statistics (*C*-stat).

### Appendix A.2.1: Spectra of events D and B

The duration of the D event is short ( $\sim 150$  s), so we estimate the background using both the standard polynomial fit to off-source intervals ( $-300$  to  $-200$  s and  $150$  to  $250$  s), and the orbital background method (above 40 keV). The model parameters from both methods are consistent within uncertainties. We report the photon index and flux (10 keV–40 MeV) for the power-law model, and the cutoff energy  $E_{\text{cut}}$  for the cutoff power-law model. We do not observe a significant statistical improvement from introducing a high-energy cutoff ( $\Delta \text{stat} = -4$ , for one additional free parameter).

Similarly to D, event B also has a short duration ( $\sim 150$  s), so both background estimation methods are applied, yielding comparable results. For wider energy coverage, we use the standard off-source intervals (2350–2550 s and 3000–3055 s). The cutoff power-law model gives only a marginal improvement in fit quality ( $\Delta \text{stat} = -14$ , for one additional free parameter).

Given that the background at the highest energies ( $>200$  keV) is well described by the orbital method, and that the detector response remains stable between events D and B, we estimate the cumulative D+B spectrum ( $>200$  keV, detector b1) for improved spectral characterization. The corresponding power-law fit is included in Table A.1.

### Appendix A.2.2: Spectrum of event E

The E outburst lasts at least 600 s. Therefore, we adopt the orbital background method (30 orbits). We model the spectrum using both power-law and cutoff power-law models. The latter does not significantly improve the spectral characterization in the 40 keV – 40 MeV range ( $\Delta \text{stat} = 1$ ).

Name	Time-bin [s]	Power-law model			Cutoff Power-law	
		Photon index	Flux [ $\times 10^{-7}$ erg cm $^{-2}$ s $^{-1}$ ]	stat(dof)	$E_{\text{cut}}$ [MeV]	stat(dof)
D	( $-100, 50$ )	$1.48 \pm 0.06$	$2.7^{+0.6}_{-0.4}$	208(235)	$> 4$	204(234)
B	(2750, 2850)	$1.47 \pm 0.05$	$2.7^{+0.4}_{-0.3}$	253(235)	$7^{+13}_{-6}$	239(234)
E*	(11200, 11800)	$1.64 \pm 0.04$	$0.56^{+0.04}_{-0.05}$	289(215)	$> 14$	288(214)
D+B**		$1.77^{+0.17}_{-0.12}$	$1.61^{+0.08}_{-0.50}$	125(119)		

Table A.1: Spectral fit results for selected time bins using power-law and cutoff power-law models. Data between 10 keV and 40 MeV and the standard off-source background estimate is applied to D and B. For the spectrum E, an average orbital method is applied and thus spectrum at 40 keV – 40 MeV is extracted. For the cumulative D+B spectrum, we have used the average orbital background method and the spectrum at 200 keV – 40 MeV is extracted. The reported flux is evaluated at the covered energy band.

## Appendix B: X-rays

### Appendix B.1: *Swift*/XRT data analysis

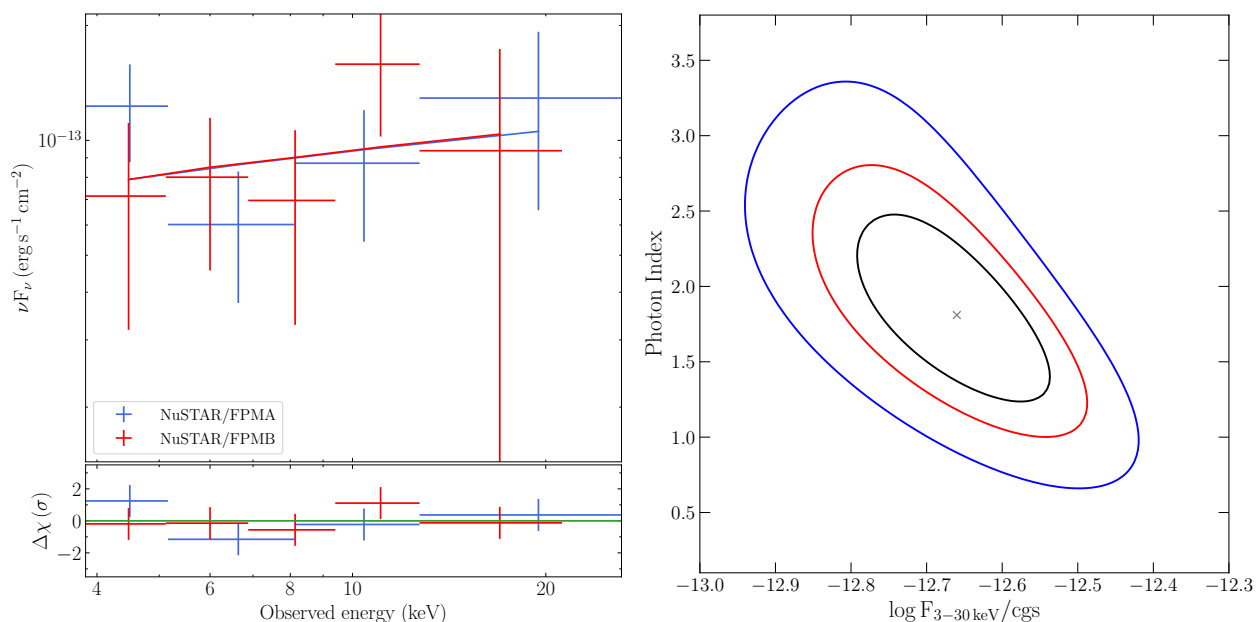
To extract the spectra, we downloaded the XRT event files from the *Swift*-XRT archive<sup>7</sup>. We extracted source and background spectra in each time bin using the *xselect* tool. For each time bin, the ancillary response has been generated by *xrtmkarf*. We then model 9 spectra with an absorbed power-law model with two neutral hydrogen absorbers: one fixed to Galactic the equivalent hydrogen column density at  $N_{\text{H}} = 0.207 \times 10^{22}$  cm $^{-2}$  and the other at the host galaxy. We have adopted 4 different redshifts for the host galaxy: 0, 0.5, 1 and 2. The equivalent hydrogen column density in the host galaxy is best fitted by  $N_{\text{H}}^{z=0} = (0.8 \pm 0.2) \times 10^{22}$  cm $^{-2}$ ,  $N_{\text{H}}^{z=0.5} = (2.2 \pm 0.6) \times 10^{22}$  cm $^{-2}$ ,  $N_{\text{H}}^{z=1} = (4.6 \pm 1.0) \times 10^{22}$  cm $^{-2}$ , and  $N_{\text{H}}^{z=2} = (13.0 \pm 3.0) \times 10^{22}$  cm $^{-2}$ . We have verified that the inferred unabsorbed flux is not affected by the choice of the redshift. And so, we report the unabsorbed 0.3 – 10 keV flux ( $z = 0$ ) and the photon index in the Table B.1.

<sup>5</sup> <https://heasarc.gsfc.nasa.gov/W3Browse/fermi/fermigdays.html>

<sup>6</sup> <https://fermi.gsfc.nasa.gov/ssc/data/analysis/gbm/DOCUMENTATION.html>

<sup>7</sup> <http://www.swift.ac.uk/archive/>

$T_{\text{start}}$ (days)	$T_{\text{stop}}$ (days)	Flux ( $10^{-11}$ erg cm $^{-2}$ s $^{-1}$ )	Photon Index
0.54	0.55	$12.35^{+1.50}_{-1.30}$	$1.61^{+0.23}_{-0.22}$
0.58	0.59	$3.53^{+0.84}_{-0.62}$	$1.90^{+0.36}_{-0.34}$
0.73	0.74	$7.59^{+1.15}_{-0.91}$	$1.78^{+0.24}_{-0.23}$
0.795	0.798	$3.50^{+0.85}_{-0.71}$	$1.37 \pm 0.40$
1.30	1.31	$1.64^{+0.45}_{-0.36}$	$1.40^{+0.47}_{-0.47}$
1.37	1.39	$1.33^{+0.28}_{-0.20}$	$1.90^{+0.33}_{-0.31}$
1.44	1.45	$1.33^{+0.32}_{-0.25}$	$1.83^{+0.40}_{-0.38}$
2.22	2.36	$0.39^{+0.11}_{-0.08}$	$1.90^{+0.40}_{-0.38}$
5.33	5.41	$0.10^{+0.17}_{-0.04}$	$2.24^{+1.25}_{-1.22}$

Table B.1: The result of the time-resolved spectral analysis of *Swift*/XRT data.Appendix B.2: *NuSTAR* data analysisFig. B.1: Left: *NuSTAR* FPMA and FPMB (blue and red, respectively) spectra fitted with a power-law model. Right: The confidence contours (68%, 95%, and 99%) of the photon index versus the 3 – 30 keV flux.

A *NuSTAR* (Harrison et al. 2013) DDT observation of DBE took place on 2025 July 12 (ObsID 91101324002; PI: E. Kamoun) for a total exposure of 39 ks. The data were reduced using the standard pipeline in the *NuSTAR* Data Analysis Software (*NuSTARDAS* v2.1.4), and using CalDB20250521. We cleaned the unfiltered event files with the standard depth correction. We reprocessed the data using the `saamode = strict`, `saacalc=3`, and `tentacle = yes` criteria for a more conservative treatment of the high background levels near the South Atlantic Anomaly. Due to the high background activity during the observation, this filtering scheme reduced our net exposure time to 31.7 ks and 32.8 ks, for the two focal plane modules (FPMA and FPMB), respectively. We extracted the source spectra from a circular region of radius 40'' centered at the coordinates of the source, using the *HEASOFT* task `nuproducts`. Background spectra were extracted from a source-free region of radius 80''. We analyze the spectra from FPMA and FPMB jointly, without combining them. The *NuSTAR* spectra were binned using the `ftgroup` task with `groupsize=optmin` and `groupscale = 25`. This sets up a binning using optimal binning as described by Kaastra & Bleeker (2016), but with the additional requirement of a minimum number of 25 counts per bin.

We modeled the *NuSTAR* spectra in the 3 – 30 keV range using *XSPEC*. We assumed an absorbed power law, by fixing the equivalent hydrogen column density at  $N_{\text{H}} = 10^{22}$  cm $^{-2}$  (assumed at  $z = 0$ , consistent with the analysis of *Swift*/XRT). We let the photon index and the normalization free to vary. This model results in a statistically good fit ( $C/\text{dof} = 5/7$ ) with a photon index of  $1.8^{+0.7}_{-0.6}$  and 3 – 30 keV flux  $\log F_{3-30} = -12.66 \pm 0.14$ . Extrapolating the best fit to the *Swift*/XRT soft band results in an unabsorbed flux in the 0.3 – 10 keV range of  $\log F_{0.3-10} = -12.6^{+0.5}_{-0.3}$ . The left panel of Fig. B.1 shows the *NuSTAR* spectra with the best-fit model. The right panel of the same figure shows the photon index versus flux contours.

## Appendix C: Fermi/LAT

We performed unbinned likelihood analysis of *Fermi*/LAT data for the  $\gamma$ -ray burst, starting from the 5 ks before the *Fermi*/GBM trigger time of GRB 250702D ( $t_0=773154547$  s MET) and expanding up to  $t_0+15$  ks seconds, in the energy range of 0.1–1 GeV, using the GTBURST<sup>8</sup> software from Fermi Science tool. We selected the region of interest covering  $12^\circ$  around the source location R.A. =  $284.69^\circ$ , Dec= $-7.87^\circ$  (J2000) consistent with the *Swift*/XRT and EP observations (Cheng et al. 2025; Kennea et al. 2025). A standard zenith angle (Zd) cut of  $100^\circ$  is applied to remove any contamination of photons from the Earth-limb. We used the P8R3\_TRANSIENT020 event class, which is suitable for transient-source analysis, and the corresponding instrument response functions. Isotropic particle background (‘isotr template’ in GTBURST), galactic and extragalactic high-energy components from the Fermi Fourth Catalog (4FGL), with fixed normalization (‘template (fixed norm)’) has been used. No significant emission during the transients was detected. We estimated a  $3\sigma$  (99.7%) upper-limit of the energy-flux while fitting a power-law (‘powerlaw2’ spectral model using GTBURST).

In addition, we computed the probability of association of photons with the burst in the given time interval using the *gtsrcprob* module in an energy range of 0.1-100 GeV. Figure C.1 shows the photons detected by LAT during this period and probability of photons associated with the transient. We detected a photon with an energy of 1.85 GeV with a probability greater than 88% of being associated with the source.

Due to the unavailability of good quality data during the flares observed by GBM mentioned in Tab. A.1, we selected a time-range starting from  $-4800$  s before the trigger to derive the flux upper-limits for two different durations of 100 s and 300 s (see Tab. C.1) in the energy range 0.1-1 GeV.

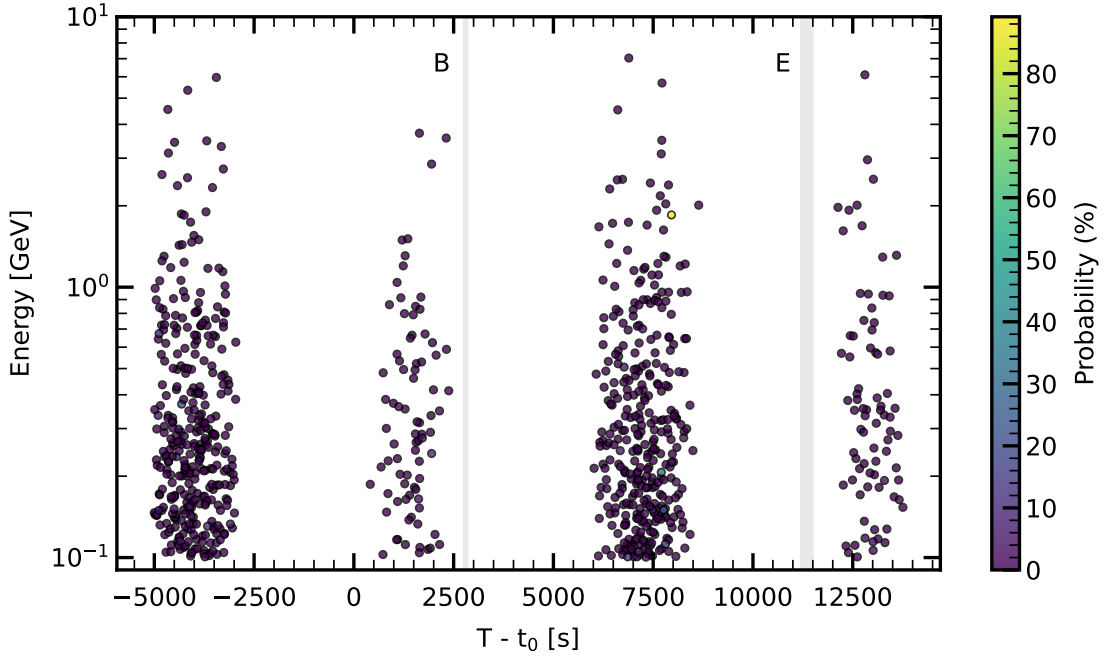


Fig. C.1: GeV photon detected by LAT from the location of GRB 250702D/B/E and probability of association with the transient. The figure shows the time-windows in which high-energy photons were detected by LAT from the transient location. The color bar represents the the probability of association of photons to the transient detected during  $t_0 - 5$  ks to  $t_0 + 15$  ks. The gray shaded region represents GRB 250702B/E. Note that LAT observed event E for approximately half of its emission period. Thus, the time interval marked by the shaded region corresponds to only half of the LAT observation.

Duration [s]	Analysis period (T- $t_0$ )	$\Gamma = -2$ [ $\text{erg cm}^{-2} \text{s}^{-1}$ ]	$\Gamma = -2.5$ [ $\text{erg cm}^{-2} \text{s}^{-1}$ ]
100	-4800, -4700	$6.8 \times 10^{-9}$	$6.7 \times 10^{-9}$
300	-4800, -4500	$3 \times 10^{-9}$	$3.1 \times 10^{-9}$

Table C.1: Upper limits in the 0.1 – 1 GeV range at the  $3\sigma$  level. Given that DBE was not covered with LAT during the burst periods, we estimated these upper limits one orbit before at the same position of the sky for two different exposures of 100 s and 300 s.

<sup>8</sup> <https://fermi.gsfc.nasa.gov/ssc/data/analysis/scitools/gtburst.html>

## Appendix D: Physical constraints

If the high-energy emission is produced via external inverse Compton (IC) scattering of thermal photons from an accretion disk, then electrons with energies<sup>9</sup>  $\gamma_e m_e c^2 \sim (E_{\max}/E_d)^{1/2} m_e c^2 \sim 3 \text{ GeV} (E_{\max,7.6}/E_{d,0})^{1/2}$  are required, where  $E_{\max}$  is the observed maximum energy and  $E_d$  is the disk photon energy, both in units of eV. For such low energies in electrons, the efficient IC cooling would require large energy density in seed photons. To ensure high radiative efficiency, the IC cooling timescale  $t'_{\text{IC}} \sim 3m_e c / (4U'_\gamma \gamma_e \sigma_T)$  must be comparable to the shell crossing time  $R/c\Gamma$ . Assuming the disk luminosity  $L_d$  is a fraction  $\eta$  of the observed luminosity  $L_\gamma$ , this condition implies  $\eta > 5 \times 10^{-5} \Gamma_1^5 \delta t_{v,2} L_{\gamma,48}^{-1}$ . Efficient IC cooling would then require  $L_d \sim 10^{43} \text{ erg s}^{-1}$ . Another possibility to produce MeV photons is via synchrotron self Compton cooling of relativistic electrons. The constraints on the seed synchrotron photons  $E_s < 10 \text{ keV}$  return weak requirements for the electron energies of  $\gamma_e m_e c^2 > 7 \text{ MeV} (E_{\max,7.6}/E_{\min,4})^{1/2}$ , the luminosity  $\eta_s \geq 2 \times 10^{-4} \gamma_{e,3}^{-1} \delta t_{v,2} \Gamma_1^5 L_{\gamma,48}^{-1}$  and magnetic field of  $B' < 7 \times 10^4 \text{ G} E_{\min,4} \gamma_3^{-2} \Gamma_1^{-1}$ . However, the inverse Compton scenario is limited in the radiative efficiency, provided lower energies in electrons.

Producing the observed MeV emission through synchrotron radiation requires  $\gamma_e \sim 10^7 \Gamma_1^{-1/2} (\epsilon/\epsilon_{\max})^{1/2} B'^{-1/2}$ , where  $B'$  is the magnetic field in the comoving frame of the emission region and  $\Gamma_1 = \Gamma/10$ . The synchrotron cooling time scale,  $t'_{\text{sync}} \sim 6\pi m_e c / \gamma_e B'^2 \sigma_T \sim$  should be shorter than the light crossing time than the emission region,  $t'_{\text{dyn}} \sim R/c\Gamma$ , where  $\delta t_{v,2} = \delta t_v/100 \text{ s}$ . For  $\epsilon = \epsilon_0 \sim 2.6 \times 10^{-4} \epsilon_{\max}$ , the condition  $t'_{\text{sync}} < R/c\Gamma$  will imply  $B' > 1 \text{ G} \gamma_{e,4.5}^{-1/2} \delta t_{v,2}^{-1/2} \Gamma_1^{-1/2}$ . Requiring the observed luminosity in  $\gamma$ -rays does not exceed the Poynting flux, we obtain  $B' < 2 \times 10^3 \text{ G} L_\gamma^{1/2} \delta t_{v,2}^{-1} \Gamma_1^{-3}$ . Therefore, sub-TeV electrons ( $\gamma_e \sim 3 \times 10^5 B_3'^{-1/2}$ ) can account for the observed spectra of DBE.

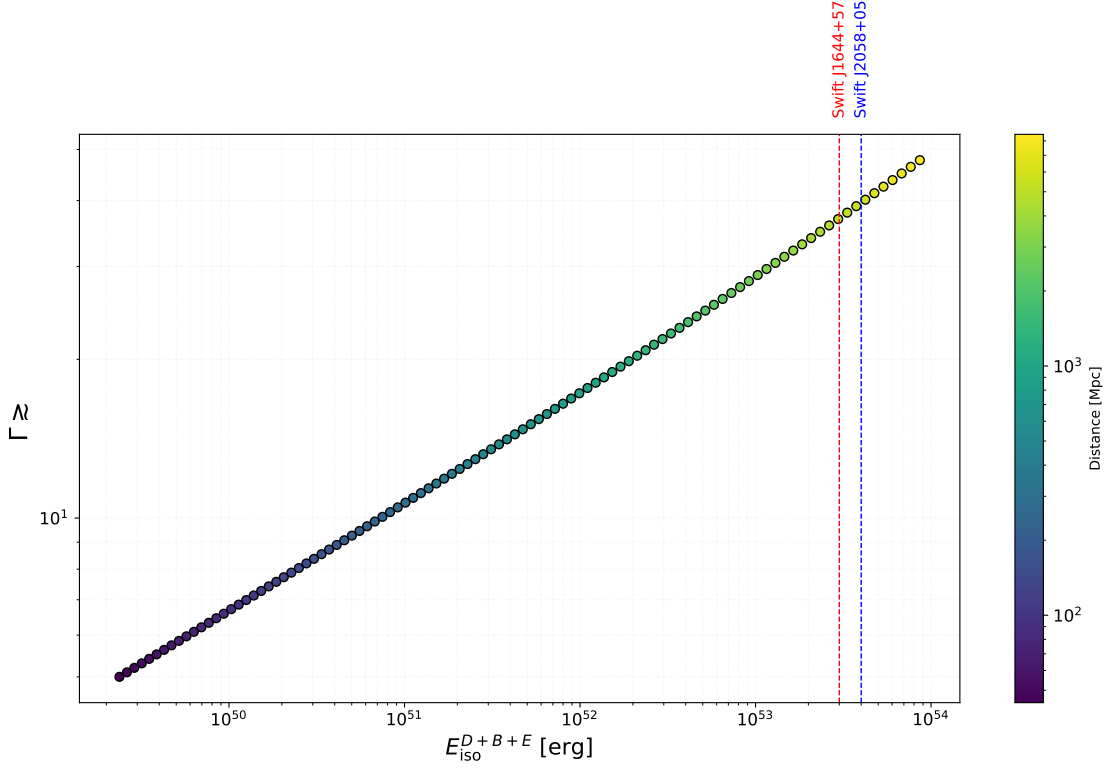


Fig. D.1: Lower limit on the bulk Lorentz factor as a function of the isotropic-equivalent energy released during all three episodes. The color bar indicates the corresponding luminosity distance to DBE. For comparison, we show total isotropic-equivalent energy measured for Swift J2058+05 (Cenko et al. 2012; Pasham et al. 2015) and Swift J1644+57 (Burrows et al. 2011) as dashed blue and red vertical lines.

<sup>9</sup> We adopt notation  $Q=10^x Q_x$  and cgs units. The photon energies instead are measured in eV.